RESEARCH ARTICLE

Key Points:
- Demonstrating the feasibility of generating satellite surface T-S diagrams
- Analyzing the dynamics of SSS with respect to in situ measurements
- Assessing additional satellite geophysical signals not resolved by Argo data

Correspondence to:
R. Sabia,
roberto.sabia@esa.int

A first estimation of SMOS-based ocean surface T-S diagrams

Roberto Sabia[1], Marlene Klockmann[2,3], Diego Fernández-Prieto[2], and Craig Donlon[4]

[1]Telespazio-Vega UK Ltd, European Space Agency, ESTEC, Noordwijk, Netherlands, [2]European Space Agency, ESRIN, Frascati, Italy, [3]Max Planck Institute for Meteorology, International Max Planck Research School on Earth System Modelling, Hamburg, Germany, [4]European Space Agency, ESTEC, Noordwijk, Netherlands

Abstract A first estimation of satellite-based ocean surface T-S diagrams is performed by using SMOS Sea Surface Salinity (SSS) and OSTIA Sea Surface Temperature (SST) and comparing them with in situ measurements interpolated fields obtained by the Argo-buoys for the North Atlantic and over the entire year 2011. The key objectives at the base of this study are: (1) To demonstrate the feasibility of generating routinely satellite-derived surface T-S diagrams, obviating the lack of extensive sampling of the surface open ocean, (2) To display the T-S diagrams variability and the distribution/dynamics of SSS, altogether with SST and the relative density with respect to in situ measurements, and (3) To assess the SMOS SSS data added value in detecting geophysical signals not sensed/resolved by the Argo measurements. To perform the latter analysis, the satellite-Argo mismatches have been overlapped with geophysical parameters of precipitation rates, surface heat and freshwater fluxes and wind speed data. Ongoing and future efforts focus on enlarging the study area and the temporal frame of the analysis and aim at developing a method for the systematic identification of surface water masses formation areas by remotely sensed data.

1. Introduction and Motivation

In the upper ocean, above approximately 500 m depth, both temperature (T) and salinity (S) variability is highest (largely driven by wind-induced turbulence and precipitation), decreasing in turn considerably below depths of 500–1000m. The potential temperature (θ, free of adiabatic warming at depth) is linked to salinity in the θ-S diagrams, which are traditionally used to analyze the relationship between observations of ocean temperature and salinity and relate them to the corresponding potential density (σ_θ). θ-S diagrams are normally derived from a broad collection of spatial and temporal in situ measurements (typically from vertical profiles), and they provide a tool to identify and characterize ocean water masses beneath the mixed layer having specific conservative "signatures." These data can be used to track the movement of water masses and to determine to which extent different water masses have mixed with each other. Water within the mixed layer has in turn nonconservative properties, because T and S values are modified by exposure to the atmosphere and mixing processes, such as solar heating or surface cooling (leading to stratification/convection), river runoff, precipitation/evaporation, ice melting/freezing and water advection and mixing. In certain areas, strong frontal patterns exist on scales of a few to hundreds of km that separate surface waters of very different density characteristics. At the ocean surface, Temperature-Salinity (T-S) diagrams relate therefore T and S to the density (σ_t) at atmospheric pressure, whereas at the ocean surface $\sigma_\theta = \sigma_t$. In this sense, surface T-S diagrams are potential tools to evaluate Sea Surface Salinity (SSS) distribution and dynamics, alongside with the mutual variation of Sea Surface Temperature (SST), as the components determining σ_t. In this context, the major relevance of the surface seawater density lies in being the triggering driver of the thermohaline circulation, a fundamental mechanism for the heat redistribution all over the oceans and the atmosphere.

The approach followed in this study is to rely on satellite estimates of T and S to estimate surface-layer T-S diagrams. Despite the lesser accuracy with respect to in situ measurements, satellite observations allow to obtain a synoptic view of broad geographical areas, with frequent temporal coverage. At microwave frequencies, in particular, remotely sensed data may be collected in all-weather conditions, day and night, and with a moderate resolution. This is particularly relevant in remote regions or in areas where in situ estimates suffer heavily from poor sampling or extensive data interpolation. In this context, The European Space Agency (ESA) Soil Moisture and Ocean Salinity (SMOS) [*Font et al.*, 2010] satellite mission is providing

space-borne observations of Sea Surface Salinity (SSS) with global coverage and sampling frequency of at most 3 days. The SMOS mission was launched in November 2009 and, following satellite and instrument commissioning activities, has provided a continuous stream of data well suited to large-scale oceanography since May 2010. The SMOS Microwave Imaging Radiometer using Aperture Synthesis (MIRAS) instrument measures brightness temperature (T_B) at L-Band (centred around 1.4 GHz) from multiple incidence angles using 64 antennae located on three equi-spaced arms which synthesize a large-diameter virtual antenna that would have been impractical to be flown in space [*McMullan et al.*, 2008]. The SSS is retrieved with an iterative inversion scheme [*Zine et al.*, 2008], capitalizing from the multiangular T_B estimates and a priori knowledge on auxiliary parameters of SST and Wind Speed (WS). The latter is required to account for ocean surface roughness that impacts the emissivity of the ocean surface at L-band frequencies. Additional corrections are required to account for Galactic, cosmic, solar radiation and Faraday rotation on the water-leaving signals measured by MIRAS after passing through the earth atmosphere. A full description of the SSS retrieval is provided in *Font et al.* [2013]. To reduce MIRAS measurements' noise and meet the challenging mission requirements (0.1 psu accuracy in salinity for a 10–30 day average for an open ocean area of 100–200 Km), SMOS single satellite overpasses are then spatio-temporally averaged over the corresponding grid cells in the appropriate temporal window (Level 3 product).

Using satellite SSS and SST measurements it is now possible for the first time to derive satellite-based surface T-S signatures on a global scale and to assess also their temporal evolution and (co-)variability. Clearly satellite estimates are related only to the surface layer and infer the nonconservative surface T-S properties of the ocean. However, as noted previously, the ocean surface is the crucial layer where T-S properties are modified through contact with the atmosphere and the ocean mixed layer plays a critical role in water mass formation.

Within this context, the main objectives of this study are:

1. to demonstrate the potential offered by satellite-derived SST and SSS to compute surface T-S diagrams, obviating the lack of extensive and routinary sampling of the surface open ocean;

2. to evaluate the satellite-based T-S diagrams variability and characterize the distribution and dynamics of remotely sensed SSS and SST through comparison to existing in situ data sets;

3. to assess the unique information that SMOS SSS data are providing with respect to those measurements, in view of a better understanding of the processes modifying seawater characteristics and governing the distribution and variability of SSS.

In *Sabia et al.* [2012], a first attempt to estimate surface-layer T-S diagrams based on satellite measurements has been conducted. Satellite derived T-S data were compared to the World Ocean Atlas 2009 (WOA09) climatology [*Locarnini et al.*, 2010; *Antonov et al.*, 2010]. In *Klockmann et al.* [2013], some experimental satellite-based T-S diagrams have been routinely derived for the year 2011 and compared with those computed from Argo-floats interpolated fields [*Gaillard et al.*, 2009], referring to a customized partition of the global ocean into seven regions, following the water mass classification of *Emery* [2003]. Subsequently, *Sabia et al.* [2013] used satellite T-S diagrams as a diagnostic tool to evaluate the temporal variation of SST and SSS (and their corresponding density); the emphasis was on a first interpretation of the geographical deviations with respect to Argo measurements, trying to distinguish between the SSS retrieval errors and the additional information contained in the satellite data with respect to Argo.

In the present study, T-S diagrams are produced from SMOS Optimally Interpolated (OI) SSS Level 3 products [*Font et al.*, 2012] and the Operational Sea Surface Temperature and Sea Ice Analysis (OSTIA) SST product [*Donlon et al.*, 2011], referring to a new partitioning of the ocean areas in the North Atlantic. The satellite-based T-S diagrams are compared with Argo-based T-S diagrams which use SST and SSS from the Near Real Time ARIVO monthly fields using the In Situ Analysis System (ISAS) [*Gaillard et al.*, 2009] interpolation scheme (in the following referred to as Argo ISAS). In order to relate the computed mismatches to identifiable oceanographic structures and processes, additional satellite data sets of evaporation/precipitation fluxes, and wind speed fields have been superimposed and their variability analyzed.

In section 2, the data sets used in this study and the methodology applied will be presented. Subsequently, in section 3, the various results will be discussed. Finally, in section 4 major findings and concluding remarks will be presented, along with a reference to the ongoing activities and an outline of the future work envisaged.
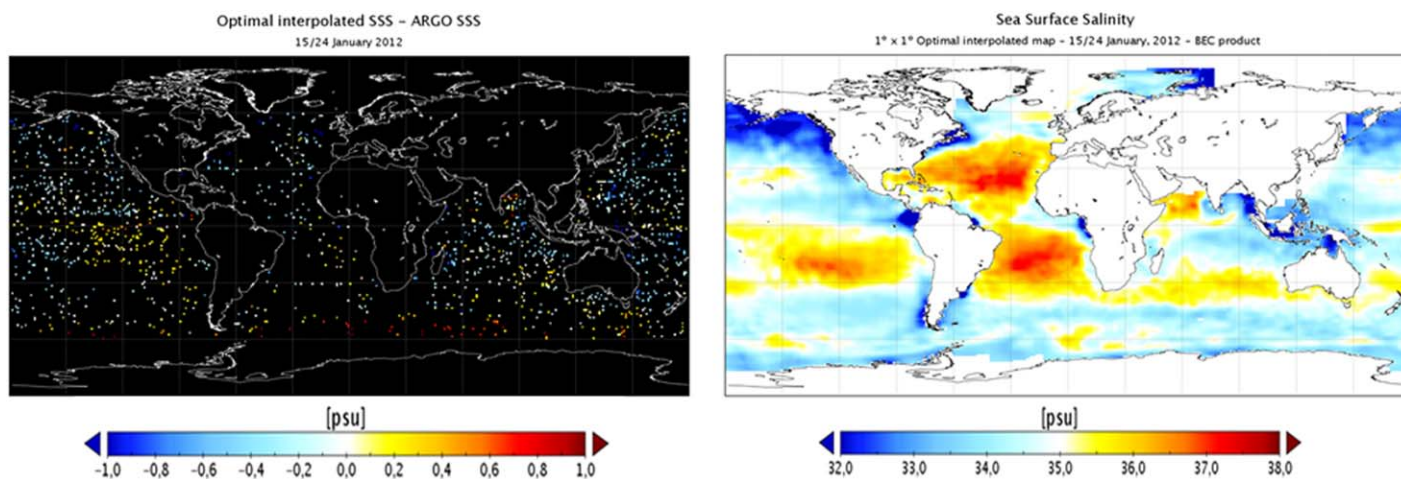
Figure 1. SMOS OI average difference with respect to Argo-floats SSS, in a 10 day sampling period in January 2012 at the Argo floats location (left), highlighting the poor coverage in certain ocean regions when compared to the 10 day SSS composite derived by SMOS (right) in the same interval (credits: J. Martinez, SMOS-BEC).

2. Data Sets and Methodology

This section lists all the data sets used in this study and the methodologies applied to address the objectives stated in the introductory section.

Concerning the SSS data sets, monthly SMOS L3 OI products collected by the SMOS-BEC data centre [*Font et al.*, 2012] have been used, with a spatial resolution of 1° by 1° computed from ascending passes obtained with the SMOS L2 processor v550 using the third roughness model (which improved the salinity retrieval under high wind speed conditions [*Guimbard et al.*, 2012]). With respect to SST, the OSTIA data set provides daily foundation temperature fields (i.e., free of diurnal variability and representing a "daily mean" SST) derived from the satellites of the Group of High Resolution SST (GHRSST) project, merged with in situ observations and optimally interpolated to a grid with 1/20° resolution [*Donlon et al.*, 2011].

As a comparative ground-truth data set, Argo-float OI fields have been collected; they are constituted by the Near Real Time Argo profiles provided by Coriolis, quality-checked and interpolated onto a regular grid in combination with other local arrays (mooring and CTD data) using the In Situ Analysis System (ISAS) [*Gaillard*, 2012]. Monthly fields are provided with a 0.25° by 0.25° resolution at the equator, with the latitudinal resolution increasing toward the poles. In the first part of the study, as said, these Argo-interpolated fields constitute the validation reference against which the satellite products are evaluated, as customary in the SMOS SSS community [e.g., *Boutin et al.*, 2012]. It has to be noted, however, that Argo floats measure at several metres depth, whilst the SMOS SSS measurements sense the very first centimetres of the ocean surface, thus some decoupling of the signals due to vertical salinity gradients in the first few meters cannot be excluded, as will be discussed in the second part of the study. Nonetheless, over specific areas and periods the Argo sampling can be poor (Figure 1), rendering the representativity of the interpolated fields in those areas sometimes questionable (stressing even more the relevance of a continuous stream of satellite data).

To perform the additional analyses for the second part of the study that will be described in section 3, NOAA CMORPH (CPC MORPHing technique) precipitation [*Joyce et al.*, 2004] and OAFlux evaporation [*Yu et al.*, 2008] have been considered. Wind speed fields have also been collected, namely from the Special Sensor Microwave Imager Sounder (SSM/IS) [see e.g., *Wentz*, 1997], using the data from satellite F17. Surface heat fluxes have been taken from the NOCS Flux data set V.2 [*Berry and Kent*, 2009] which are based on the International Comprehensive Ocean-Atmosphere Data Set (ICOADS) data.

In *Sabia et al.* [2012] and *Klockmann et al.* [2013], the global ocean was divided into seven ocean basins. In this paper the test area is in turn restricted to the North Atlantic ocean, with the aim of focusing on a lesser number of zones representing different SST and SSS regimes characterized by specific T-S properties. The
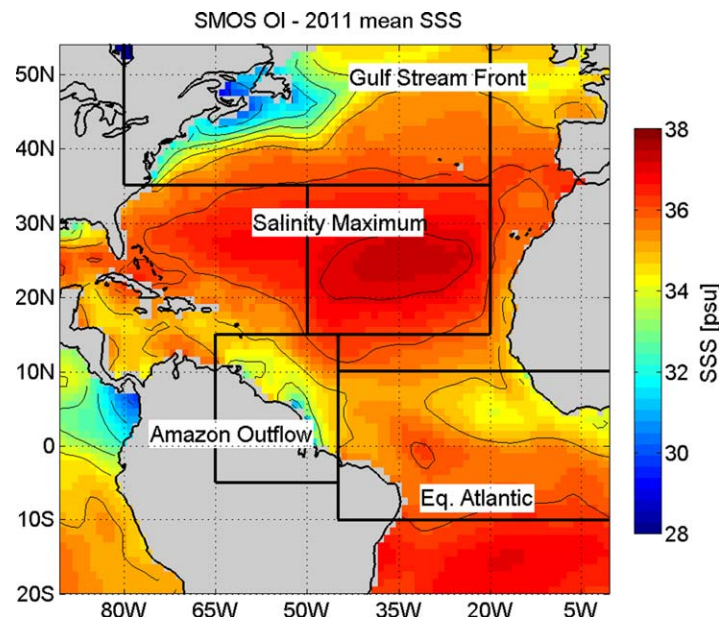
Figure 2. Study area in the North Atlantic encompassing the four subregions under study: the Gulf Stream Front (GSF), the Salinity Maximum (SM), the Amazonas Outflow (AMZ) and the Equatorial Atlantic (EQA). Superimposed, monthly (September 2011) sample SSS as measured by SMOS over the area.

study area spans the North Atlantic from 55°N to 20°S, sampled monthly during the whole year 2011. Within this area, four subregions have been defined experiencing as many different regimes (Figure 2):

1. Gulf Stream Front (GSF)— large SST and SSS gradients with the impact of overpassing synoptic weather systems;

2. Salinity Maximum (SM)—the subtropical regime with high SSS, strong evaporation, very small gradients of SSS and SST, corresponding to the recent SPURS experiment field campaigns [*Qu et al.*, 2013];

3. Amazon outflow (AMZ)— small SST range, in correspondence of the freshwater plumes of two large rivers (the Amazonas and the Orinoco), with consequently large gradients and high temporal variability in SSS and

4. Equatorial Atlantic (EQA)—the tropical regime with strong precipitation resulting from atmospheric deep convection.

For each subregion, SST is plotted against SSS, both for monthly and seasonally averaged data. The corresponding density is calculated using the equation of state TEOS10 [*McDougall and Barker*, 2011]. The satellite-based T-S diagrams have been compared to the Argo ISAS data under the assumptions described above. Besides, in order to evaluate the difference between the satellite and in situ data at any given point in space, the differences between OSTIA and Argo ISAS SST (ΔSST) and between SMOS and Argo ISAS SSS (ΔSSS), respectively, have been calculated and plotted.

3. Results and Discussion

3.1. T-S Diagrams

As anticipated in the introduction, the first part of the study deals with the derivation of satellite surface T-S diagrams, analysing their temporal variability and the distribution and dynamics of the single components, by using Argo-interpolated data as a validation test bed. In Figure 3, the surface T-S diagrams for both satellite and in situ measurements have been computed and displayed for the four subregions under study and the different seasons in 2011.

Satellite data are depicted with blue dots, while Argo ISAS data are represented in red dots, with the isopycnals superimposed. The SSS, SST and density dynamics in the various geographical regions is described afterward.

The SST over the Gulf Stream front ranges from 2.5 to 20°C and SSS from 32 to 36.5 psu in winter, where colder SST is connected with fresher SSS (concomitant occurrences of low SST at high latitudes and freshening most-likely due to inputs from the Labrador current flow and subpolar gyre and residual sea-ice flowing out of the Labrador sea). They mostly show an isopycnal development, with small density range in spite of the large SSS and SST excursions (compensating each other in terms of buoyancy). In summer, SST is shifted toward warmer temperatures with a range from 12 to 28°C. Most points have a salinity between 34 and 37 psu. There are scattered SSS points between 30 and 34 psu, observed in both Argo ISAS and SMOS, with the
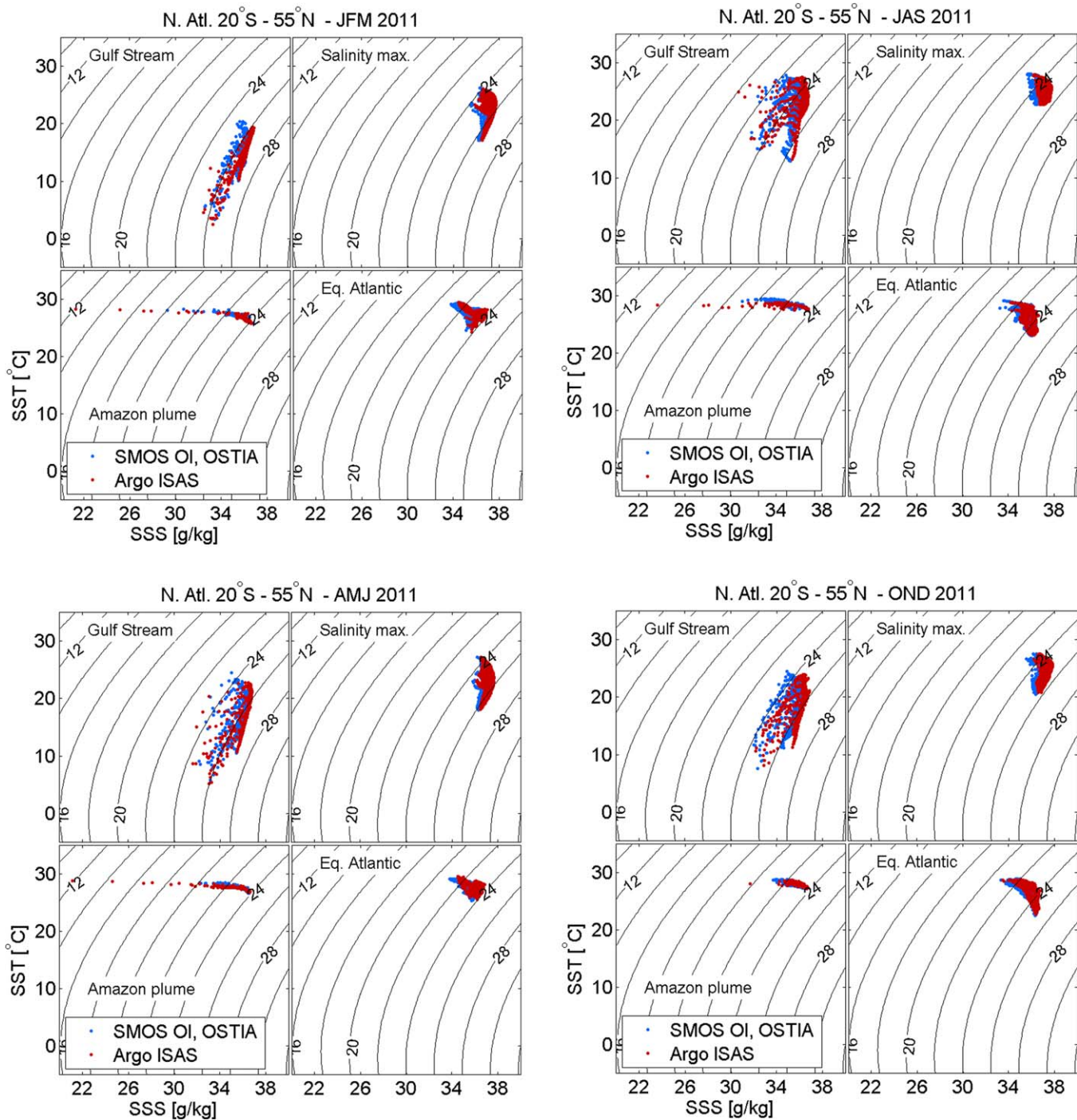
Figure 3. Seasonal averages of T-S diagrams comparing satellite data (blue dots) and Argo ISAS data (red dots) in the four subregions considered: (top left) GSF, (top right) SM, (bottom left) AMZ, (bottom right) EQA, during winter (JFM), spring (AMJ), summer (JJA) and autumn (OND) seasons of 2011. Isopycnals are superimposed.

latter tending again to be systematically fresher. In general, the greatest deviation between satellite and in situ measurements appears to be in this region, where time/space variability introduced by baroclinic instability and eddy shedding contributes to large differences between the near-surface and the subsurface.

Over the Salinity Maximum, the T-S signature exhibits very little scatter. The SST range is larger during winter (17–27°C) than during summer (22–29°C) months. The SSS maximum is located at 38 psu, and SMOS appears up to 1 psu fresher, indicating that evaporation is not the only parameter influencing surface salinity in this region.

Besides, in the AMZ region the temperature range is very small, with SST being all year round between 25 and 28°, and with OSTIA somewhat warmer in the JAS period. SSS largely ranges from 37 psu to as fresh as 22 psu (except during OND), with a clear diapycnal (crossing isopycnals) signature, in which the large density range is mostly driven by salinity; SMOS tends to be a little fresher but without reproducing the very fresh Argo outliers (these points are however located close to the coast, where the Argo sampling is poor and therefore such Argo OI pixels are questionable). The smallest SSS range (from 37 to 34 psu) is found during OND with very few fresher points. This corresponds well with the seasonal cycle of the river discharge of the Amazon and Orinoco [*Dai et al.*, 2009]. The discharge is maximum in May/June (July/August) for the Amazon (Orinoco) and minimum in October/November (February/March) for the Amazon (Orinoco).

Lastly, in the equatorial Atlantic the T-S signature is quite stable with a SST maximum of 29/30°C which is at the same time in correspondence with the minimum in SSS at 34 psu. The maximum SSS is at 37 psu with SST around 28°C. SST shows a minimum at 25°C with SSS between 35 and 36 psu. In summer there is no such clear min/max structure, but the ranges remain unchanged. In general, the SMOS satellite estimations turn out to be fresher than the Argo ISAS fields, most likely in relation to the heavy rainfall regimes experienced in this area.

In terms of the sea surface density (SSσ), denser water with SS$\sigma > 24$ kg/m3 is present at the Gulf Stream front and at the Salinity Maximum. The densest water is found during the winter months at the Gulf Stream front exceeding 27 kg/m3, essentially driven by the cold waters found in this area. Over the Amazon/Orinoco outflow and the equatorial Atlantic the density ranges between 21 and 24 kg/m^3 or is even smaller in case of the Amazon/Orinoco outflow in summer.

As mentioned, for the comparisons with Argo OI fields, the differences between OSTIA SST and Argo ISAS SST (ΔSST) and between SMOS SSS and Argo ISAS SSS (ΔSSS), respectively, have been calculated, plotting ΔSST against ΔSSS. Figure 4 shows an example of the relative mismatch of the satellite and Argo data in the respective regions and seasons considered. It can be noticed how these differences stretch over different parts of these mismatch diagrams, highlighting and inspecting how this difference can have a more pronounced SST or SSS component. Overall, however, there is a systematic freshening detected by SMOS with respect to Argo ISAS, which will be analyzed more in detail in the second part of the study. In Table 1, the mean values and standard deviations of the ensemble of points belonging to each subregion are listed for each of the four seasons. In the following, special attention will be paid to the performances relevant to the SSS and the relative mismatch with the Argo data.

The Gulf Stream front and the Equatorial Atlantic show similar performances with a mean misfit varying between −0.25 and −0.47 psu, while the accuracy lies between 0.23 and 0.35. More accurate performances are found over the Salinity Maximum area; here the accuracy is about 0.15 both in winter and in summer. One reason for the high accuracy is surely the absence of any land contamination and the warm temperatures throughout the year. In winter there is a small mean misfit of −0.13 psu while in summer it is of −0.32 psu. Lastly, the Amazon/Orinoco outflow shows a low accuracy with respect to Argo ISAS (a standard deviation of 1.38 psu in winter and 2.14 psu in summer) but the mean misfit is very close to zero.

To close the evaluation of the SSS distribution alongside with the SST, the corresponding density has been calculated for both SMOS and OSTIA data and also for Argo-OI fields, and their average difference computed and plot in Figure 5 to evaluate its geographical patterns, over the entire North Atlantic encompassing the four area under study for the four seasons of the year 2011.

Positive density anomaly patches (SMOS/OSTIA estimated to be denser than the Argo ISAS fields) appear to be quite consistent in the Equatorial Atlantic for the entire year, with an attenuation only in winter. The SM also experiences a dramatic increase in positive values in winter; analysing the Figure 4 this density anomaly seems to be SST-driven (remarkable lower SST sensed by OSTIA).

Conversely, negative density anomaly patches (SMOS/OSTIA estimated to be lighter than the Argo ISAS fields) appear in the Gulf Stream area and in the AMZ, quite constantly all over the year. Again looking at the Figure 4, they seem to be mostly SSS-driven, but the SST influence can also be significant (especially in the GSF) due to the variability introduced by baroclinic instabilities. Concerning the AMZ, the small positive anomaly patch (high SSS anomaly) is thought to be related to a poor Argo sampling close to the coast and
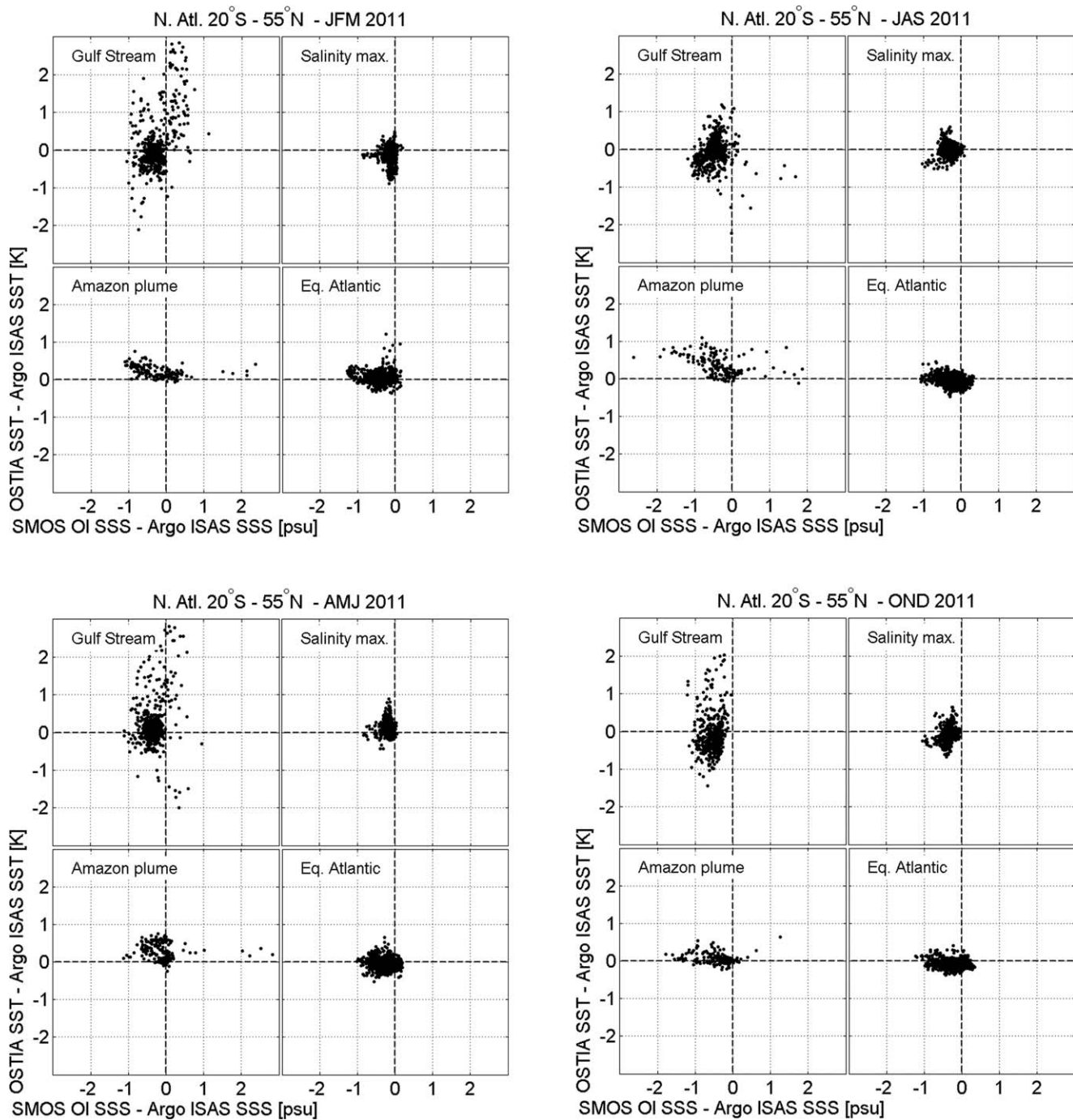
Figure 4. Same as Figure 3, but for the seasonal averages of SST differences (ΔSST) versus SSS differences (ΔSSS).

the consequent unreliable Argo ISAS fields, generating spurious substantial differences with the satellite products.

In general, the slightly negative density anomaly (pale blue) which characterize all the subplots can be related to the systematic freshening mentioned in Figure 4.

3.2. Mismatches and Geophysical Signals

In the previous experiments the approach has been to evaluate/determine the T-S diagrams, the relative mismatches and the density anomalies using the Argo-interpolated fields as a ground-truth validation products.

Table 1. Mean Misfit and Standard Deviation (Accuracy) of the Satellite Measurements With Respect to Argo ISAS for Both the ΔSSS and the ΔSST for Each Zone and Season Considered

Zones/Seasons	Parameter	JFM	AMJ	JAS	OND
Gulf Stream Front (GSF)	mean(dSSS) − psu	−0.26	−0.33	−0.48	−0.52
	std(dSSS) − psu	0.32	0.26	0.29	0.20
	mean(dSST) − K	0.12	0.25	−0.07	−0.10
	std(dSST) − K	0.76	0.70	0.37	0.50
Salinity Maximum (SM)	mean(dSSS) − psu	−0.13	−0.18	−0.32	−0.33
	std(dSSS) − psu	0.14	0.11	0.15	0.14
	mean(dSST) − K	−0.11	0.14	0.00	−0.08
	std(dSST) − K	0.21	0.18	0.16	0.18
Amazon Outflow (AMZ)	mean(dSSS) − psu	−0.07	0.10	−0.08	−0.46
	std(dSSS) − psu	1.07	1.51	1.57	0.55
	mean(dSST) − K	0.21	0.27	0.35	0.07
	std(dSST) − K	0.15	0.22	0.27	0.14
Equatorial Atlantic (EQA)	mean(Dsss) − psu	−0.39	−0.36	−0.26	−0.29
	std(dSSS) − psu	0.27	0.23	0.28	0.29
	mean(dSST) − K	0.06	−0.05	−0.05	−0.07
	std(dSST) − K	0.16	0.15	0.14	0.11

With this approach, therefore, the errors estimated would be entirely ascribable to the satellite biases/inaccuracies (due to e.g., the roughness models applied in the SSS retrieval at L-band, artificial contaminations such as land-contamination or RFI, or external noise sources such as Galactic noise and Sun glint [*Font et al.*, 2010]).

In the second part of the study, the latter consideration is challenged, under the assumption that the errors quantified in Figure 4 would embed both the actual satellite inaccuracies but also relevant geophysical signals detected by the satellites and not revealed/resolved by the Argo fields, mainly because of their different depth sampling. Therefore, the computed mismatches will be compared with a selection of geophysical parameters which influence the SSS distribution and retrieval, to assess whether some kind of correlation exists and the satellite is actually sensing an additional valuable information which is only mistakenly deemed as errors.

Following this, and in order to display the mismatches computed above and shown in Figure 4, a classification criterion can be defined to assist the interpretation. The approach chosen is to derive a combined mismatch by calculating a mismatch radius (overall mismatch regardless of its source) and a mismatch angle ϕ (mismatch phase in the ΔSST-ΔSSS domain) as follows:

$$R = \sqrt{(\Delta SST^2 + \Delta SSS^2)} \tag{1}$$

$$\varphi = \tan^{-1}(\Delta SST/\Delta SSS) \tag{2}$$

Figure 6 shows the classification of the combined mismatch using Eqn. (1) and (2). Four classes are distinguished: overestimation of SST and SSS by the satellites with respect to Argo ISAS (blue), underestimation of SST and SSS (yellow), overestimation of SST and underestimation of SSS (cyan) and underestimation of SST with overestimation of SSS (red). White colour indicates a mismatch radius smaller than a chosen threshold of 0.5, whilst light green marks points that have a large mismatch radius which is almost entirely induced by SST (whose investigation is outside the scope of this paper). Figure 6 shows an example for the distribution of quadrants for the month of August 2011.

This combined mismatch index allows to plot these discrepancies geographically and inspect visually the regions of interest. As an example, in Figure 7, the colour-coded quadrants of the combined mismatch are shown using SMOS satellite measurements for the entire 2011 represented in the four different seasons. Superimposed are precipitation rate contours from the CMORPH data set, with the contour interval set at 3 mm/d, starting at 3 mm/d. The colour intensity reflects the magnitude of the mismatch radius. As it can be seen, in some area there is a relatively good spatial agreement between areas of large negative ΔSSS (marked cyan and yellow) and areas where P exceeds 3 mm/d on a seasonal average, especially over the Gulf Stream and in the equatorial Atlantic. There are, however, several areas where SMOS shows a fresher signal and the monthly average precipitation is below 3mm/d (albeit not much evident during spring). This can be either geophysical, for instance in the mismatch patterns located in the region of the Amazon/Orinoco outflow where P is low and the mismatch is therefore most likely dominated by river runoff, but also instrumental or Argo-related, such as the high SST anomaly close to the coast depicted in cyan mostly related to the poor Argo coverage close to the coast. This indicates that the freshwater signal is not necessarily the only signal
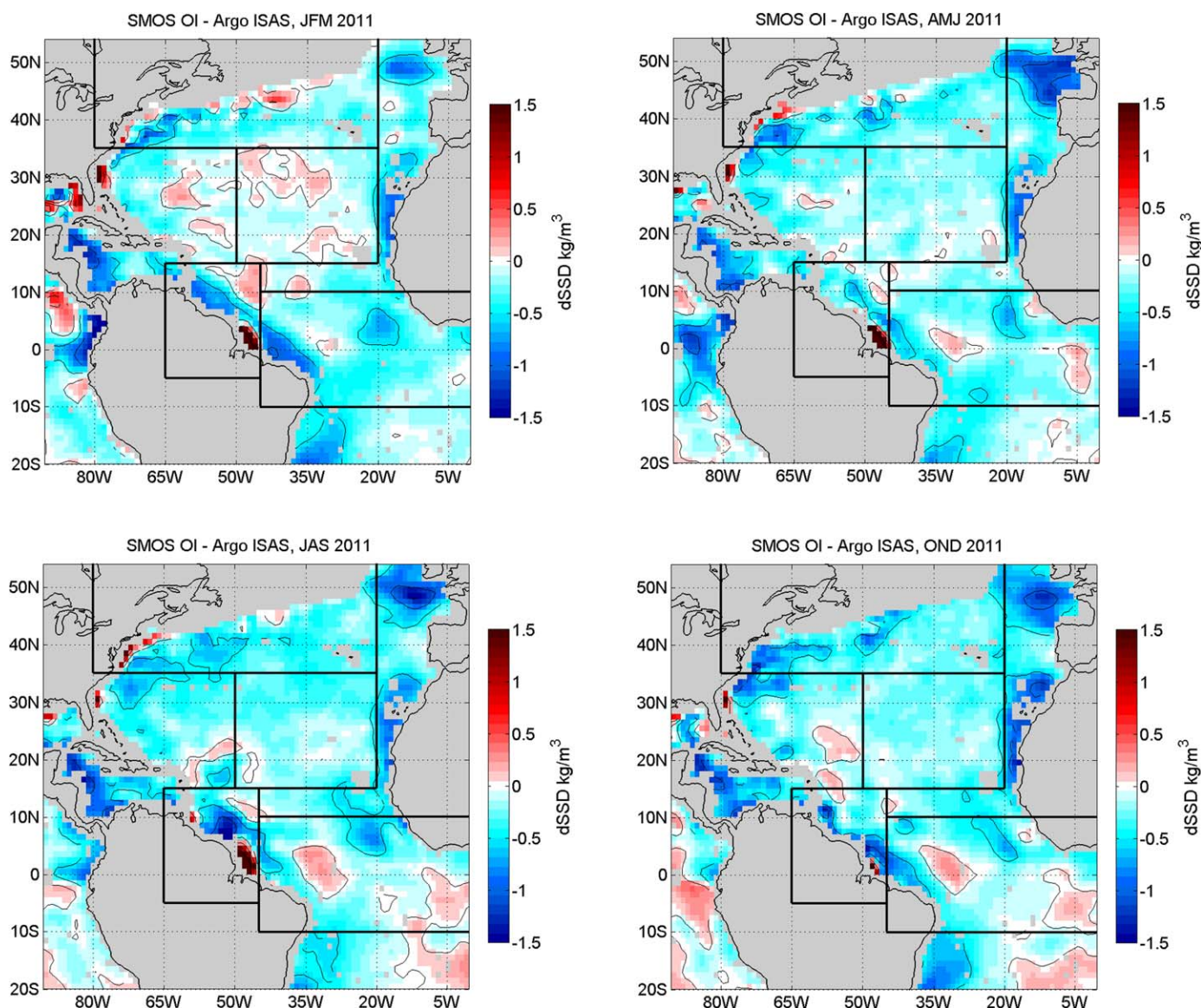
Figure 5. Density anomaly field geographical patterns, over the entire North Atlantic encompassing the four areas under study for the four seasons of the year 2011.

picked by the satellite estimates and also that some precipitations rates can be smoothed along the seasonal temporal window.

The opposite also happens (precipitation not associated to a detected freshening), even if this can also be related to the choice of the coloured threshold. Some of the large mismatches near the continents may be due to land-contamination which has been reduced but is still present in the reprocessed SMOS data.

With the attempt of highlighting the effect of certain geophysical parameters on the SMOS signal, the following figures focus on the effect of a single specific parameter at a time and relate it to the SMOS-Argo ISAS discrepancies. Again, some part of these discrepancies might be caused by near-surface stratification, since satellites are measuring salinity at about 1-cm depth while the Argo floats stop measuring near 5 m depth. The relevant parameters under consideration are averaged over bins of ΔSST and ΔSSS and the figures are generated for the whole North Atlantic area. The parameters considered in the following are precipitation, net surface heat and freshwater fluxes and 10 m wind speed.

Figure 8 displays the precipitation rate from the CMORPH data set as a function of ΔSST and ΔSSS for SMOS mismatches for the period spanning the whole 2011. Fresh SSS anomalies go down to about -1.5 psu,
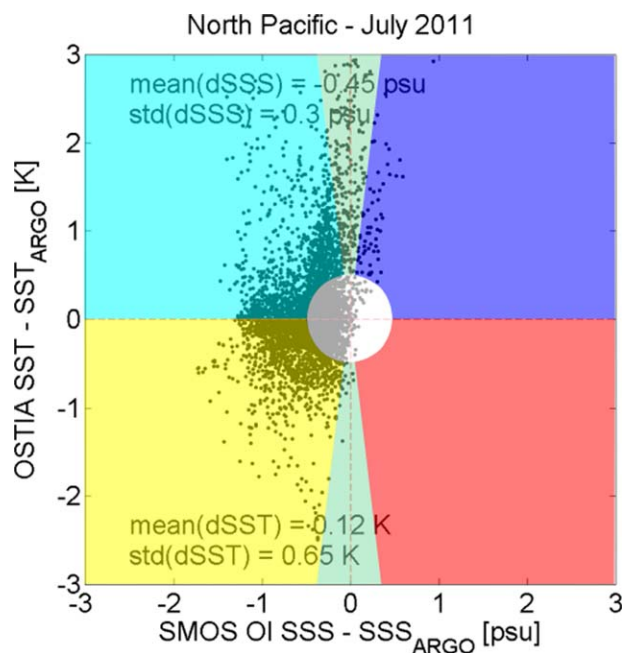
Figure 6. Classification of the combined mismatch into four different quadrants: overestimation of SST and SSS by the satellites with respect to Argo ISAS (blue), underestimation of SST and SSS (yellow), overestimation of SST and underestimation of SSS (cyan), and underestimation of SST with overestimation of SSS (red). White colour indicates a mismatch radius smaller than the chosen threshold of 0.5; light green mark points that have an SST-induced large mismatch radius.

clearly showing how the bin-averaged precipitation is increasing toward negative ΔSSS, i.e., when $SSS_{SMOS} < SSS_{Argo}$ (SMOS sensing freshwater lenses due to the higher P). The isolines of P are orientated almost vertically which indicates that ΔSST is basically not influenced by precipitation (at least not with respect to Argo ISAS); that is, at equal ΔSSS the precipitation pattern does not seem to change much, whilst the opposite happens at equal ΔSST. As discussed above, SMOS shows fresher anomalies also in areas with little to no precipitation (e.g., over the Salinity maximum), which supports the consideration that only part of the fresher signal can be explained by precipitation and that the detected mismatches are the sum of actual inaccuracies and geophysical signals.

A fresh SMOS mean misfit with respect to Argo-interpolated data was expected, as also found in previous studies [e.g., *Boutin et al.*, 2013]. In that paper, the authors find that the distribution of SMOS SSS – Argo SS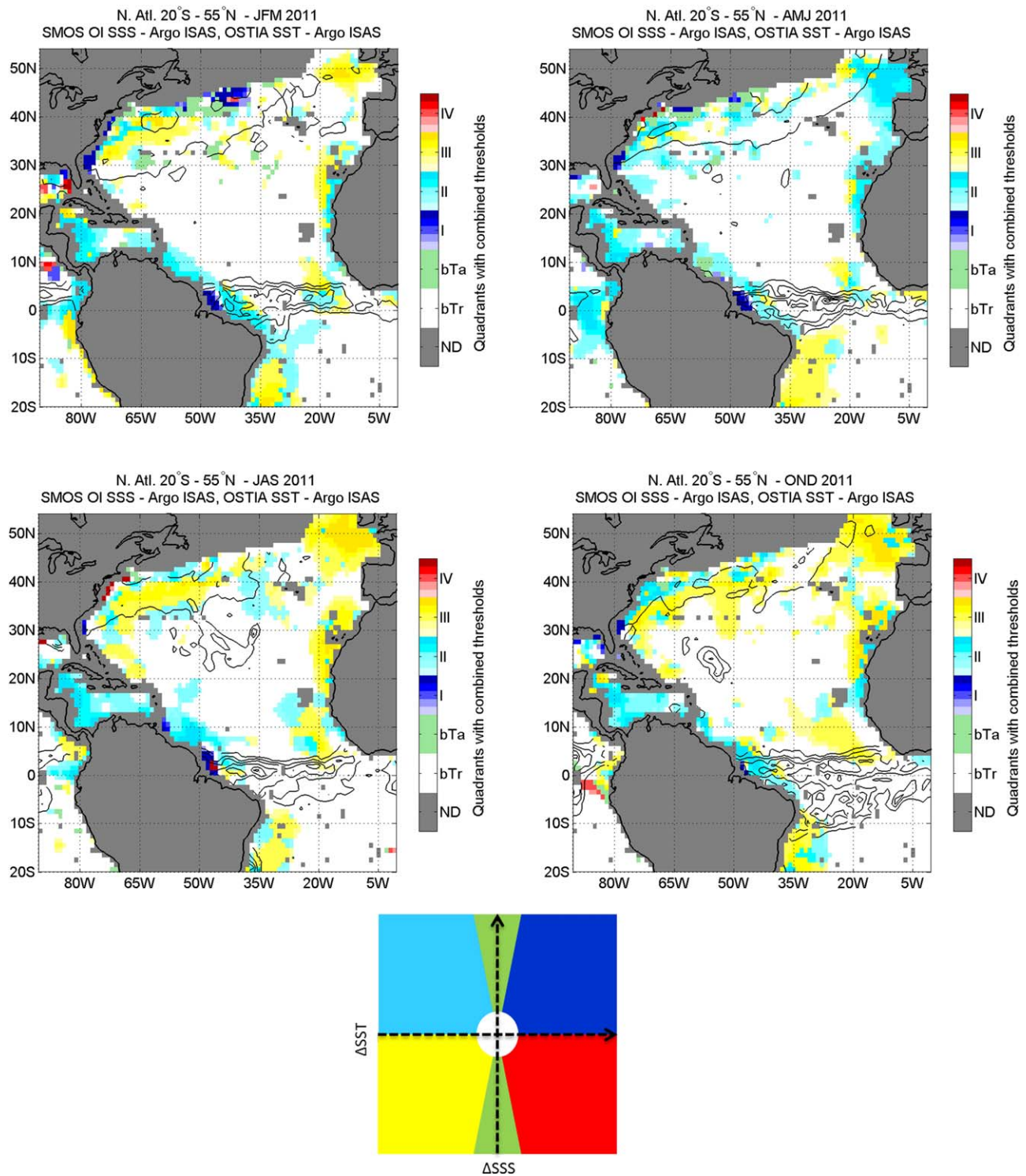S is shifted toward negative values; this negative mean misfit is reduced if SMOS measurements coinciding with rainfall pixels are removed. Such fresh misfit may be evidence for a near-surface stratification (freshwater lenses) during and shortly after rain events. When comparing to *Boutin et al.* [2013], the SMOS freshening detected in this study is however too high to be explained by precipitation only. The effect of rainfall on SSS and SST has also been explored by *Reverdin et al.* [2012] analysing surface drifter data. They find an average drop in salinity at 50 cm depth of about 0.6 psu associated with precipitation, where about 30 % of the cases lie between 0.2 and 0.5 psu and other 30 % are above 0.5 reaching up to 2 psu. Data from drifters which measured at 50 cm and 15 cm depth suggest that the anomalies increase toward the surface, suggesting that the initial drop in SSS directly at the surface may also be exceeding the average of 0.6 psu measured at 50 cm depth, in line with the detected SMOS-Argo ISAS differences. Furthermore, *McCulloch et al.* [2012] suggest that rain lenses with a salinity anomaly of 1–4 psu (depending on the roughness model) can be detected by SMOS, in agreement with the findings of *Schlüssel et al.* [1997], which predicted shallow rain lenses up to 4 psu in a vertical ocean mixing model. Since the SMOS SSS L3 OI data are obtained with the third roughness model of the official salinity processor, the salinity anomaly of the rain lenses will be reduced to 1–2 psu, as indicated by *McCulloch et al.* [2012]. The authors also suggest that the mixing of the freshwater is limited to the upper 10–15 cm, therefore rain lenses would be more likely detected by satellite measurements than by Argo floats which often measure not shallower than 5 m below the surface.

In summary, SMOS mismatch cloud is shifted toward negative ΔSSS and the effect of rain events is clearly visible in the monthly SMOS SSS fields, despite the effect of sporadic phenomena such as rain lenses on monthly averages still needs to be assessed to make the magnitude of the freshening more comparable. Furthermore, the so-called splashing effect (increased roughness detected by the instrument due to the raindrops impinging the surface) needs to be considered as well. This unaccounted enhanced roughness translates into an apparent freshening of the SSS, therefore summing up to the previous effect. This is an example of how the detected freshening can have both a geophysical and a satellite-induced component.

Figure 7. Quadrants of combined mismatch of ΔSST and ΔSSS for OSTIA SST-Argo SST and SMOS SSS-Argo SSS for the four seasons of 2011. Contours of CMORPH precipitation overlaid. The contour interval is 3 mm/d, starting from 3 mm/d. Colour intensity reflects the magnitude of the mismatch radius. The graphical colorbar resembles the color-coding chosen in Fig. 6. Pixels in gray have no data.

Figure 8 (right) also shows a scatter plot of SMOS ΔSSS as a function of binned CMORPH precipitation rate for the whole year 2011. The resulting bin-averaged ΔSSS is indicated by the light green bars. The red line represents a least squares fit of ΔSSS as a function of precipitation, and is given by:
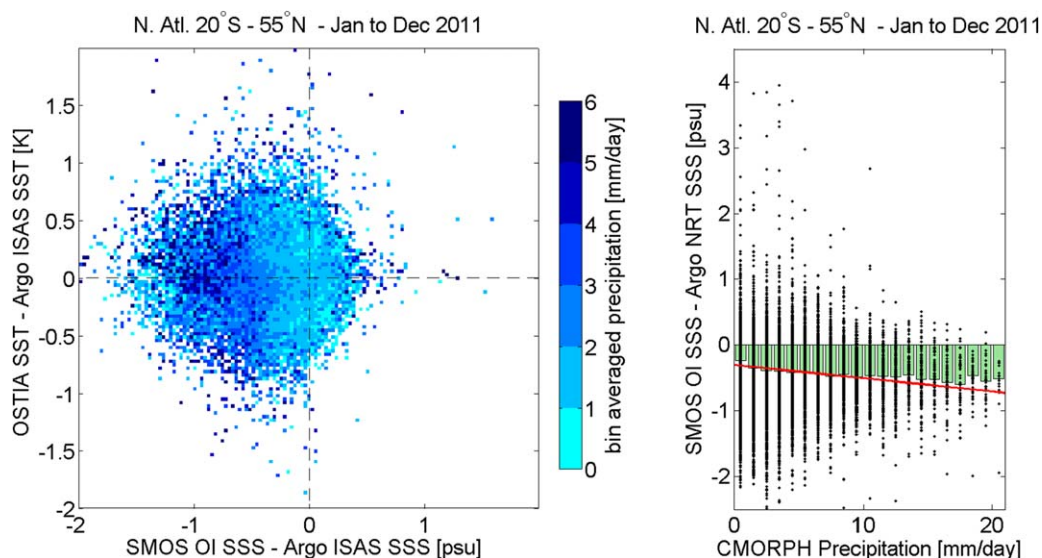
Figure 8. (left) Precipitation rates as a function of ΔSST and ΔSSS for SSS$_{SMOS}$ − SSS$_{Argo}$ and SST$_{OSTIA}$ − SST$_{Argo}$ for the whole year 2011. (right) Scatter-plot of SMOS ΔSSS per bins of CMORPH precipitation, for the whole year 2011. Light green bars indicate bin-averaged ΔSSS; the red line represents a linear fit of ΔSSS as a function of precipitation.

$$\Delta SSS = -0.02 \ RR - 0.3 \qquad\qquad (3)$$

Where *RR* indicates the rain rate in mm/d. It should be noted that, even in case of no rain, the ΔSSS would still be equal to −0.3 psu, yet another confirmation that the precipitation is not the only parameter at stake in this analysis.

As mentioned above, another set of parameters has been analyzed, namely the heat and freshwater fluxes. The heat flux data have been taken from the NOCS Surface Flux Data Set v2.0 [*Berry and Kent*, 2009], whilst the freshwater flux is calculated as the difference between the OAFlux Evaporation [*Yu et al.*, 2008] and the CMORPH precipitation [*Joyce et al.*, 2004]. In Figure 9, the ΔSST and ΔSSS as a function of the net surface heat flux (left) and net surface freshwater flux (right) are shown.

The effect of the net surface heat flux is predominantly visible in ΔSST; negative ΔSST are connected with negative heat flux, i.e., with a cooling of the ocean surface, and vice versa. Looking at the four components of the net heat flux separately (not shown) revealed that this relation is mainly due to the impact of the incoming short wave radiation. Basically, positive/negative heat fluxes (warming/cooling) are promptly detected by the OSTIA product and translate into a corresponding anomaly with respect to the Argo product. For ΔSSS the pattern is not equally clear, and the relationship of heat fluxes with SSS is not straightforward to interpret; positive heat fluxes values, however, concentrate in the positive SSS anomaly section, indicating that the surface heating is mostly associated to a higher SMOS SSS due to evaporation.

For the freshwater fluxes (E-P) the effect of ΔSSS is much more pronounced, with an overall expected pattern of fresher ΔSSS associated to negative E-P, whilst the positive E-P scatter more broadly over the ΔSSS range, even though the peak is consistently on the saltier ΔSSS side.

The fourth parameter whose influence on the combined mismatch has been studied is the 10 m height Wind Speed (WS). Figure 10 shows the effect of the SSMIS [e.g., *Wentz*, 1997] WS variation on ΔSSS and ΔSST, using SMOS again for the whole year 2011. As it can be seen, WS also shows a clear correlation to ΔSST, with larger wind speeds associated with negative ΔSST and smaller wind speeds with positive ΔSST. It is hypothesized that this is a result of the evaporative cooling effect imposed by stronger winds. Even though the correlation with ΔSST is much more straightforward, a pattern with respect to ΔSSS is also present, showing a slight diagonal trend with high WS corresponding to large SSS negative mismatch. The related explanations entail the same reasoning discussed above for the raindrop splashing effect: wind-induced enhanced roughness translates into fresher SSS estimation, but there is also a direct impact of WS
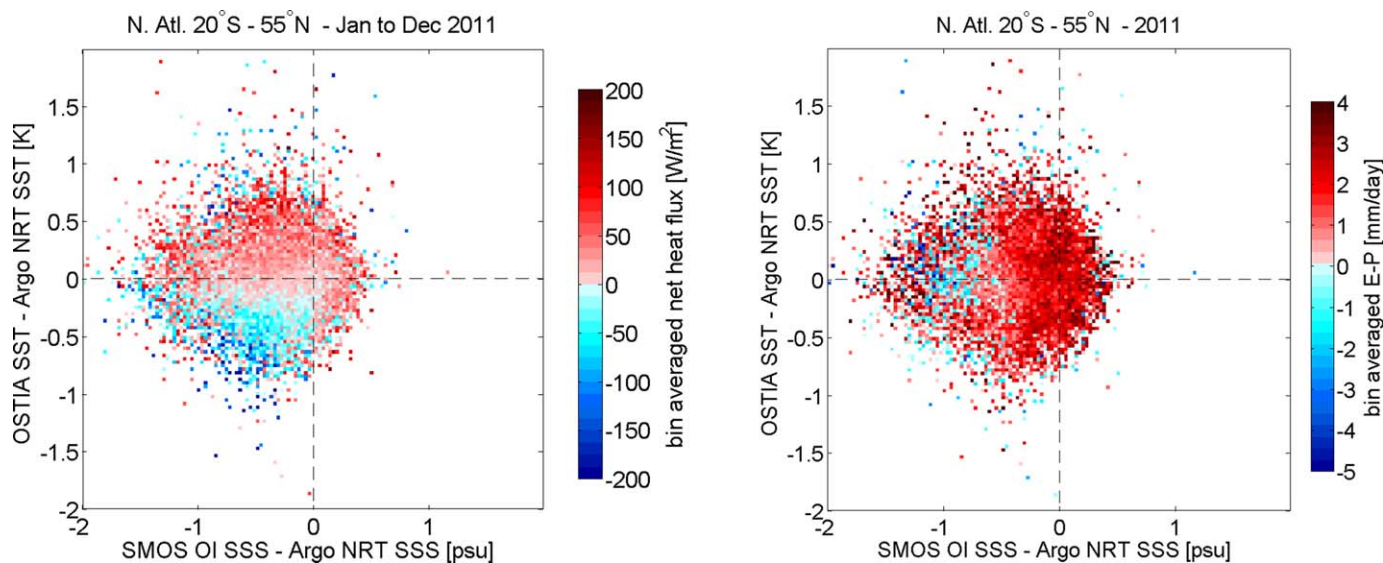
Figure 9. (left) Net surface heat flux and (right) E-P fluxes plot as a function of ΔSST and ΔSSS for the whole year 2011.

on ΔSSS by modifying the surface stratification patterns. Nevertheless, at high WS the salinity estimation in the SMOS retrieval scheme is much more challenging [e.g., *Reul et al.*, 2012; *Sabia et al.*, 2010], therefore also in this case geophysical effects and satellite retrieval inaccuracies are concomitant. Lastly, collocation of the different measurements can also be an issue, being uncertain how the spatiotemporal offsets/misalignments of WS with respect to SSS will influence the performances on monthly scales.

4. Conclusions and Future Work

The present study assessed the temporal (co-)variability of the surface T-S signature in different oceanographic regimes of the North Atlantic and compared satellite-derived SSS and SST (using SMOS and OSTIA) with in situ SSS and SST obtained from optimally interpolated maps of Argo floats measurements.
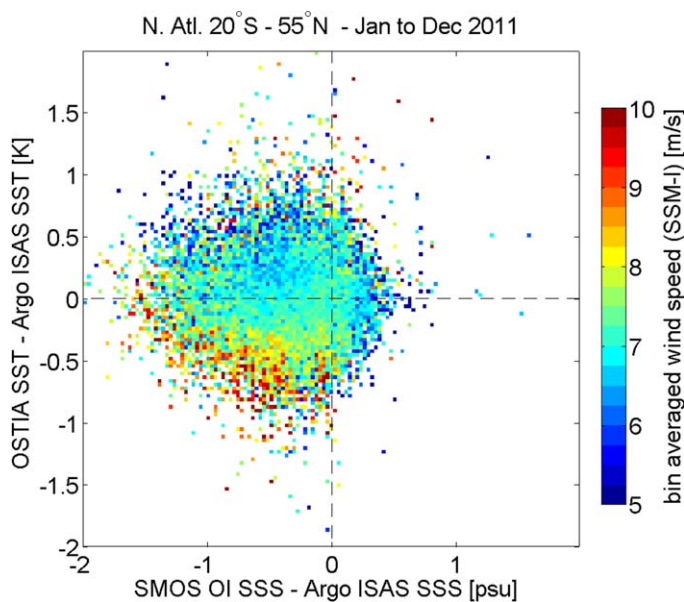

Figure 10. 10 m wind speed derived from SSMIS as a function of ΔSST and ΔSSS for SMOS SSS – Argo SSS and OSTIA SST – Argo SST for the whole year 2011.

A distinct intrinsic value of this study was to provide a dynamical view of the satellite SSS distribution in conjunction with SST, both determining the seawater density and therefore their major relevance for oceanography. Besides, the study major avenues were 1) To demonstrate the feasibility of deriving satellite-derived SST and SSS to compute surface T-S diagrams, obviating the lack of extensive and routinary sampling of the surface open ocean; 2) To evaluate the satellite-based T-S diagrams variability and characterize the distribution and dynamics of remotely sensed SSS and SST through comparison to existing Argo-interpolated fields; 3)

To assess the additional geophysical insights that the satellites are providing with respect to those measurements.

To address the latter, the relationship of ΔSSS and ΔSST to precipitation, surface fluxes and 10 m wind speed have been evaluated. SMOS showed a distinct correlation between the detected freshening and precipitation rates (and also geographically some overlapping with precipitation areas), but also a fresh misfit in areas with little to no precipitation (some of the large mismatch near the continents may be still due to land-contamination or poor Argo sampling). Together with a quantitative assessment of the rain rate impact, this suggested that only part of the fresher signal can be explained by precipitation. Additional studies have been performed to evaluate the effect of surface heat/freshwater fluxes and wind speed on the combined mismatches. As per the surface fluxes, when split into components of heat and freshwater fluxes, correlations with both ΔSST and ΔSSS were evidenced, despite the ΔSST influence is predominant. Wind speed seem also to impact more on the ΔSST, but ΔSSS signal is also present (especially at high WS), mostly likely as a concomitant effect of enhanced freshening due to roughened seas and retrieval inaccuracies in the challenging regime of high WS.

Ongoing research efforts are being devoted to various aspects of the topic. First of all, in terms of data sets used, an extensive work is foreseen in widening the focus of this study, both by using longer data sets (spanning over 2012 and 2013) to allow evaluating seasonal and interannual effects, and also by using different products coming from various satellites and production centres. For the latter, the impact of using L3 SSS products from the French CATDS centre will be evaluated, together with additional sources of SST.

Concerning the methodology applied, other classification/segmentation techniques using different criteria are being evaluated; moreover, the study is being extended to the Pacific ocean to study (by comparison) the effect of RFIs and to evaluate performances focusing also on stable areas, where, for instance, the Ocean Target Transformation (SMOS bias mitigation module) computation is performed [*Gourrion et al.*, 2012].

In terms of the geophysical parameters, whose impact against the combined satellite mismatches will need to be further assessed, additional studies will use ocean currents (e.g., OSCAR data sets) [*Bonjean and Lagerloef*, 2002] products to evaluate the impact of the horizontal advection, and more in general the different components of the salt budget will be computed to assess how they relate to the ΔSST and ΔSSS mismatch parameters. Furthermore, the analysis of the impact of wind speed will be extended by using ECMWF blended winds, being the same field used as auxiliary data in SMOS, to reduce a possible source of discrepancies in the mismatches.

Lastly, the most significant efforts are being devoted to the characterization of the water mass formation areas using satellite T-S diagrams. A T-S curve (i.e., a range of values) defines a water mass, which refers to a water body with the same formation history, occurred at the ocean surface under specific conditions determining its temperature and salinity. The idea is to link the temporally evolving surface T-S signatures to the observation of water masses and to understand which part of the surface signal is actually contributing to water mass formation, i.e., at which SSS and SST specific density classes are formed [*Speer and Tzipermann*, 1992]. The T-S diagrams can therefore become a tool to identify trends or shifts in the water masses, locate geographically their formation areas and better understand the link between the surface and deeper layers.

Eventually, studies of this kind will provide evidence of SSS biases/errors currently experienced by the satellites but also, in a wider context, will provide a means for gaining insights into buoyancy-driven phenomena and on the oceanic branch of the hydrological cycle.

References

Antonov, J. I., D. Seidov, T. P. Boyer, R. A. Locarnini, A. V. Mishonov, H. E. Garcia, O. K. Baranova, M. M. Zweng, and D. R. Johnson (2010), Volume 2: Salinity, in *World Ocean Atlas 2009, NOAA Atlas NESDIS 69*, edited by S. Levitus, 184 pp., U.S. Gov. Print. Off., Washington, D. C.

Berry, D. I., and E. C. Kent (2009), A new air-sea interaction gridded dataset from ICOADS with uncertainty estimates, *Bull. Am. Meteorol. Soc.*, *90*(5), 645–656.

Bonjean, F., and G. S. E. Lagerloef (2002), Diagnostic model and analysis of the surface currents in the tropical Pacific Ocean, *J. Phys. Oceanogr.*, *32*, 2938–2954.

Boutin, J., N. Martin, X. Yin, J. Font, N. Reul, and P. Spurgeon (2012), First assessment of SMOS data over open ocean: Part II Sea Surface Salinity, *IEEE Trans. Geosci. Remote Sens.*, *50*(5), 1662–1675, doi:10.1109/TGRS.2012.2184546.

Boutin, J., N. Martin, G. Reverdin, X. Yin, and F. Gaillard (2013), Sea surface freshening inferred from SMOS and ARGO salinity: Impact of rain, *Ocean Sci.*, *9*, 183–192.

Dai, A., T. Qian, K. E. Trenberth, and J. D. Milliman (2009), Changes in continental freshwater discharge from 1948–2004, *J. Clim.*, *22*, 2773–2791.

Donlon, C. J., M. Martin, J. D. Stark, J. Roberts-Jones, E. Fiedler, and W. Wimmer (2011), The Operational Sea Surface Temperature and Sea Ice analysis (OSTIA), *Remote Sens. Environ.*, *116*, 140–158, doi:10.1016/j.rse.2010.10.017.

Emery, W. J. (2003), *Water Types and Water Masses, Ocean Circulation*, pp. 1556–1567, Encyclopedia of Atmospheric Sciences, Elsevier Sci.

Font, J., A. Camps, A. Borges, M. Martín-Neira, J. Boutin, N. Reul, Y. H. Kerr, A. Hahne, and S. Mecklenburg (2010), SMOS: The challenging sea surface salinity measurement from space, *Proc. IEEE*, *98*, 649–665.

Font, J., et al. (2012), SMOS CP34 soil moisture and ocean salinity maps, in *12th Specialist Meeting on Microwave Radiometry and Remote Sensing of the Environment (MicroRad)*, pp. 1–4, IEEE, Microwave Radiometry and Remote Sensing of the Environment (MicroRad), Rome, Italy.

Font, J., et al. (2013), SMOS first data analysis for sea surface salinity determination, *Int. J. Remote Sens.*, *34*(9–10), 3654–3670.

Gaillard, F. (2012), ISAS-Tool Version 6: Method and configuration, Ifremer, Ref: LPO-12-02, doi:10.13155/22583.

Gaillard, F., E. Autret, V. Thierry, P. Galaup, C. Coatanoan, and T. Loubrieu (2009), Quality control of large ARGO data sets, *J. Atmos. Oceanic Technol.*, *26*(2), 337–351.

Gourrion, J., R. Sabia, M. Portabella, J. Tenerelli, S. Guimbard, and A. Camps (2012), Characterization of the SMOS instrumental error pattern correction over the ocean, *IEEE Geosci. Remote Sens. Lett.*, *9*(4), 793–797.

Guimbard, S., J. Gourrion, M. Portabella, A. Turiel, C. Gabarro, and J. Font (2012), SMOS semi-empirical ocean forward model adjustment, *IEEE Trans. Geosci. Remote Sens.*, *55*(5), 1676–1687.

Joyce, R. J., J. E. Janowiak, P. A. Arkin, and P. Xie (2004), CMORPH: A method that produces global precipitation estimates from passive microwave and infrared data at high spatial and temporal resolution, *J. Hydrometeorol.*, *5*, 487–503.

Klockmann, M., R. Sabia, D. Fernandez-Prieto, C. Donlon, M. Talone, and J. Font (2013), Satellite-based TS diagrams derived from SMOS, Aquarius and OSTIA data, paper presented at 33rd EARSeL Symposium on Towards Horizon 2020, edited by R. Lasaponara, N. Masini, M. Biscione, Earth Observation and Social Perspectives, Matera, Italy.

Locarnini, R. A., A. V. Mishonov, J. I. Antonov, T. P. Boyer, H. E. Garcia, O. K. Baranova, M. M. Zweng, and D. R. Johnson (2010), Temperature, in *World Ocean Atlas 2009, NOAA Atlas NESDIS 68*, vol. 1, edited by S. Levitus, 184 pp., U. S. Gov. Print. Off., Washington, D. C.

McCulloch, M. E., P. Spurgeon, and A. Chuprin (2012), Have mid-latitude ocean rain-lenses been seen by the SMOS satellite?, *Ocean Modell.*, *43-44*, 108–111.

McDougall, T. J., and P. M. Barker (2011), Getting started with TEOS-10 and the Gibbs Seawater (GSW) oceanographic toolbox, *SCOR/IAPSO WG127*, 28 pp.

McMullan, K. D., M. A. Brown, M. Martin-Neira, W. Rits, S. Ekholm, J. Marti, and J. Lemanczyk (2008), SMOS: The payload, *IEEE Trans. Geosci. Remote Sens.*, *46*(3), 594–605.

Qu, T., S. Gao, and I. Fukumori (2013), Formation of salinity maximum water and its contribution to the overturning circulation in the North Atlantic as revealed by a global GCM, *J. Geophys. Res. Oceans*, *118*, 1982–1994, doi:10.1002/jgrc.20152.

Reul, N., J. Tenerelli, J. Boutin, B. Chapron, F. Paul, E. Brion, F. Gaillard, and O. Archer (2012), Overview of the first SMOS Sea Surface Salinity products. Part I: Quality assessment for the second half of 2010, *IEEE Trans. Geosci. Remote Sens.*, *50*(5), 1636–1647.

Reverdin, G., S. Morisset, J. Boutin, and N. Martin (2012), Rain-induced variability of near sea-surface T and S from drifter data, *J. Geophys. Res. Oceans*, *119*, C02032, doi:10.1029/2011JC007549.

Sabia, R., A. Camps, M. Talone, M. Vall-llossera, and J. Font (2010), Determination of the Sea Surface Salinity Error Budget in the Soil Moisture and Ocean Salinity Mission, *IEEE Trans. Geosci. Remote Sens.*, *48*(4), 1684–1693.

Sabia, R., J. Ballabrera, G. Lagerloef, E. Bayler, M. Talone, Y. Chao, C. Donlon, D. Fernández-Prieto, and J. Font (2012), Derivation of an experimental satellite-based T-S diagram, Geoscience and Remote Sensing Symposium (IGARSS), IEEE International, pp. 5760–5763, Munich, Germany, doi:10.1109/IGARSS.2012.6352302.

Sabia, R., M. Klockmann, C. Donlon, D. Fernández-Prieto, M. Talone, and J. Ballabrera (2013), Satellite-based T-S diagrams: A prospective diagnostic tool to trace ocean water masses, Proc. 'Living Planet Symposium 2013', (ESA SP-722, December 2013), edited by L. Ouwehand, Published and distributed by ESA Communications, ESTEC, Noordwijk, Netherlands.

Schlüssel, P., A. V. Soloviev, and W. J. Emery (1997), Cool and freshwater skin of the ocean during rainfall, *Boundary Layer Meteorol.*, *82*, 437–472.

Speer, K., and E. Tziperman (1992), Rates of water mass transformation in the North Atlantic, *J. Phys. Oceanogr.*, *22*, 93–104.

Wentz, F. J. (1997), A well-calibrated ocean algorithm for special sensor microwave/imager, *J. Geophys. Res.*, *102*(C4), 8703–8718.

Yu, L., X. Jin, and R. A. Weller (2008), Multidecade global flux datasets from the Objectively Analyzed Air-sea Fluxes (OAFlux) Project: Latent and sensible heat fluxes, ocean evaporation, and related surface meteorological variables, *OAFlux Tech. Rep. OA-2008-01*, 64 pp., Woods Hole Oceanogr. Inst., Woods Hole, Mass.

Zine, S., et al. (2008), Overview of the SMOS Sea Surface Salinity Prototype Processor, *IEEE Trans. Geosci. Remote Sens.*, *46*(3), 621–645.